

Deep Feature Segmentation Model Driven by Hybrid Convolution Network for Hyper Spectral Image Classification

Rahul K Ghotekar¹, Kailash Shaw² and Minakhi Rout³

^{1,3}School of Computer Engineering, KIIT University, Bhubaneswar, India

²Department of AIML, Symbiosis Institute of Technology, Pune Campus, Symbiosis International (Deemed University), Pune, India

Received 1 Dec. 2023, Revised 16 Apr. 2024, Accepted 1 May 2024, Published 1 Aug. 2024

Abstract: Hyper-spectral image (HSI) classification can support different applications, such as agriculture, military, city planning, land utilization, and identifying distinct regions. It is treated as a crucial topic in the research community. Recent advancements in convolution neural networks (CNN) have shown the unique capability of extracting meaningful features and classification. However, CNN works with square images with fixed dimensions and cannot extract local information of images having distinct geometric variations with context and content relationships; hence, there is a scope for improvement in correctly identifying class boundaries. Encouraged by the facts, we propose an HSI feature segmentation model by the hybrid convolution network (GCNN-RESNET152) for the HSI classification. First, pre-trained CNN on ImageNet is used to obtain the multi-layer feature. Second, the 3D discrete wavelet transform image is fed into the graph convolution network GCN model to gain patch-to-patch correlations feature maps. Finally, the features are integrated using the concatenation method of the three-weighted coefficients. Finally, the linear classifier is used to predict the semantic classes of pixel HSI. The proposed model is tested on four benchmark datasets: Houston University (HU), Indian Pines (IP), Kennedy Space Station (KSS), and Pavia University (PU). The result is compared with state-of-art algorithms and is superior in terms of overall, average, and kappa accuracy. The Overall, average and kappa accuracy achieved for HU 93.59%, 98.25%, 91.59%, IP 99.86%, 98.84%, 99.56%, KSS 99.85%, 99.68%, 99.8%, and PU 99.95%, 99.65%, 99.7% respectively, which is 5 to 8% more than state of the art methods.

Keywords: Hybrid Convolution Network, Hyper-spectral image, classification, deep feature segmentation

1. INTRODUCTION

The recent year witnessed hyper-spectral image (HSI) classification in the military, irrigation, mining, and route detection [1], [2], as shown in **Fig 1**. Most machine learning ML algorithms such as K-nearest neighbor [3], support vector machine [4], Bayesian classifier [5], kernel-based method [6], and regression model [7] have been used for HSI classification [8], [9]. The major drawback of this ML is the manual extraction of features, which is time-consuming. Recently Deep learning algorithms have shown remarkable results with automatic feature extraction from raw images. HSI classification using deep learning is categorized into 1-D CNN [10], [11], 2-D CNN [12], [13], [14], and 3-D CNN [15].

The CNN model has its limitations. During the training, it stuck in local minima or gradient descent. The pooling layer can lose maximum information during pre-processing. In contrast, 3-D CNN is experienced as computationally costly and complex. On the other side, to capture the topological and geometric features of the geospatial image, the GCN model is found to be the most effective [16].

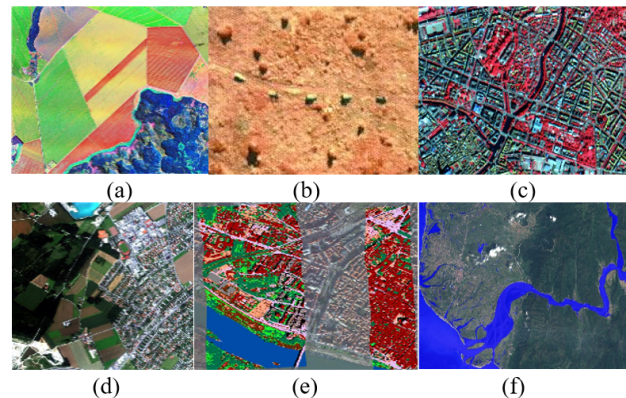


Figure 1. Real World application of Hyperspectral Image a) Corn Varieties showing HSI in agriculture [17] b) Military Surveillance or Tracking [18] c) Urban Green Observation [19] d) Land Utilization [20] e) City Planning [21] f) Flood Monitoring [22]

The CNN model [16], while a powerful tool in machine learning, does have its limitations. One notable issue arises



during the training process when the model can become trapped in local minima or struggle with gradient descent convergence. This can hinder its ability to learn and generalize effectively. Another drawback lies in the pooling layer, which, during pre-processing, can lead to the loss of maximum information, potentially affecting the model's ability to discern critical features. In contrast to the CNN, the 3-D CNN, although capable of capturing intricate spatial information, is often considered computationally expensive and complex. This increased computational burden can hinder its practicality and efficiency in certain applications.

To address these challenges and leverage the strengths of both the CNN and the GCN (Graph Convolution Network) models, we propose a novel approach—a deep feature segmentation model known as GCNN-RESNET152—for hyper-spectral image (HSI) classification. This innovative hybrid model combines the ResNet152 architecture for global feature extraction and the GCN for context feature extraction from the 3D discrete wavelet transform image. By employing GCN, we can effectively reveal patch-wise correlations within feature maps, enhancing the model's ability to understand intricate spatial relationships.

The proposed approach follows a structured workflow:

- **Global Feature Extraction (ResNet152):** Initially, we employ the ResNet152 model to extract global features from the hyper-spectral images. This step helps the model capture high-level information that is vital for accurate classification.
- **Context Feature Extraction (GCN):** Next, we utilize the Graph Convolutional Network (GCN) to extract context features from the 3D discrete wavelet transform image. This approach enables the model to capture intricate topological and geometric features of geospatial images, which are essential for precise classification.
- **Integration of Extracted Features:** Once we have both the global and context features, we integrate them using weighted methods. This fusion of information ensures that the model leverages the strengths of both feature extraction processes, enhancing its overall classification performance.
- **Classification with Linear Classifiers:** The integrated features are then used to train and test a linear classifier. We explore various classifiers, including Support Vector Machine, Decision Tree, Naïve Bayes, K-Nearest Neighbors (KNN), and Extreme Machine Learning.
- Remarkably, our experimental results demonstrate that the Extreme Machine Learning classifier consistently outperforms the other classifiers in terms of classification accuracy. This indicates the effectiveness of our proposed hybrid model in providing

discriminative features for accurate HSI classification.

Furthermore, we assess the overall performance of our approach by comparing its average accuracy and kappa accuracy with those of other state-of-the-art algorithms. Our results reveal that our method significantly outperforms these alternative approaches on four benchmark datasets: Indian Pines, Kennedy Space Station, Houston University, and Pavia University. This superior performance underscores the potential of the GCNN-RESNET152 model for hyper-spectral image classification tasks.

The paper is structured into seven sections. The introduction provides an overview of hyperspectral image analysis, highlighting the need for improved methods. Section 2 delves into the materials and methods, covering hyperspectral imaging, a comprehensive review, and the utilization of convolutional neural networks (CNNs), graph convolutional networks (GCNs), and 3D discrete wavelet transform (3D-DWT) for feature extraction. Section 3 presents the proposed architecture, detailing the design of the hybrid convolution network. Section 4 focuses on result analysis, including data description, experimental setup, multilayer feature extraction, feature fusion, and experiment analysis. In Section 5, the paper discusses the novelty of the approach and provides a summarization of key findings. Section 6 concludes the paper by presenting conclusions and outlining future research directions. Finally, Section 7 acknowledges contributions from individuals, organizations, or funding agencies.

2. MATERIALS AND METHODS

A. Hyper Spectral Imaging

Spectroscopy techniques play a crucial role in the field of Hyper-spectral Imaging (HSI), a powerful technology used to collect detailed information about objects or scenes. Unlike the human eye, which can perceive only three primary colors (blue, green, and red), HSI goes beyond this limitation by capturing images at numerous distinct wavelengths across a wide range, typically spanning from 01 to 1000 μm (micrometers). The fundamental concept of HSI involves breaking down the spatial area of interest into countless small regions, typically pixels. For each of these pixels, HSI records the intensity of light at multiple wavelengths. This data is then represented as a three-dimensional cube, commonly referred to as the "HSI cube."

This cube comprises three dimensions: X and Y Dimensions (Spatial Information): These represent the horizontal and vertical dimensions of the image, which correspond to its spatial extent. Essentially, it's the familiar 2D representation of the object or scene. λ Dimension (Spectral Information): This is the third dimension, which represents the spectral content or the wavelength information. It extends perpendicular to the X-Y plane. In essence, this dimension contains information about the different wavelengths of light used to capture the image. So, when you examine an HSI cube, you're looking at a composite image that combines

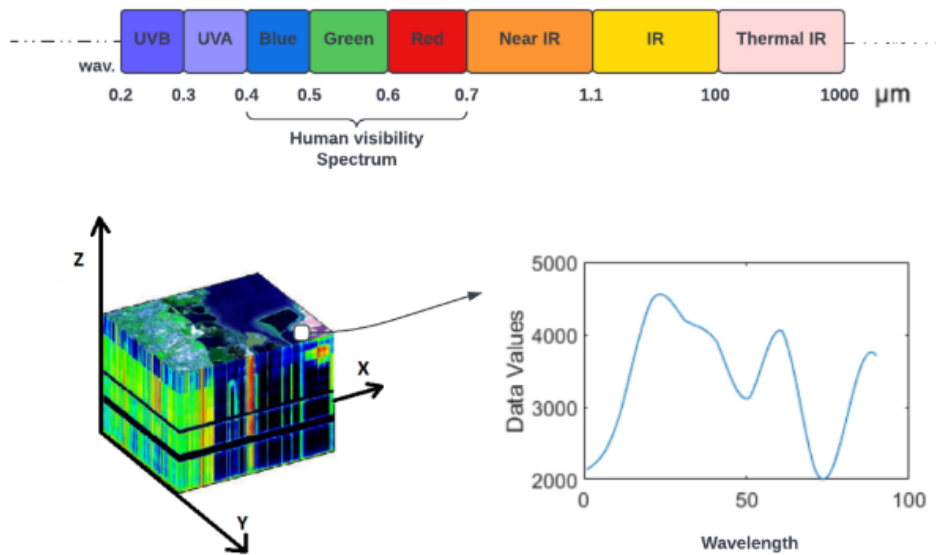


Figure 2. Pixel represents HSI, visualized as a data cube, where (x, y) axis represents spatial information and z (lambda or wavelength) axis represents spectral information of the image.

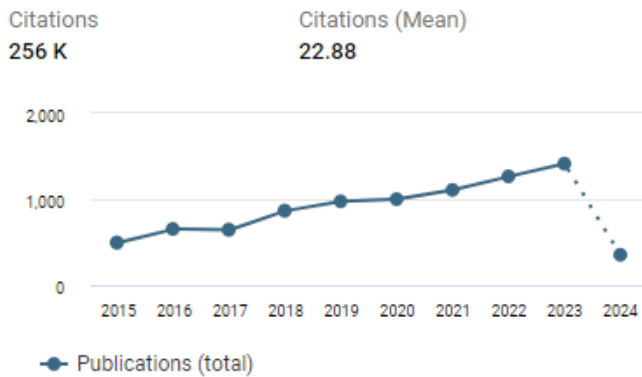


Figure 3. Total Publication Count as Per Dimensions.AI for Hyper-spectral Image Classification.

spatial and spectral information. Each pixel within the cube represents a tiny piece of the overall scene and contains data about how light at different wavelengths interacts with that specific part of the object or scene.

To provide a visual representation, **Fig 2** in illustrates this HSI cube. It's essentially a graphical depiction of the HSI data structure, with axes representing the spatial dimensions (X and Y) and the spectral dimension (λ). This cube is a fundamental concept in hyper-spectral imaging, serving as the basis for extracting valuable information about the materials, composition, and characteristics of the objects or scenes being observed. One important application of hyper-spectral imaging is the classification of objects

within the image. This involves the task of assigning a specific class label to every individual pixel in the image. This can be done using advanced machine learning and image processing techniques, allowing for the identification and analysis of specific features or materials within the scene.

B. Comprehensive Review

Over the years, from 1997 to 2024, several studies have delved into methodologies to tackle challenges in hyper-spectral image (HSI) classification, **Fig 3** depicts the total publication count in the research of HSI. [23] introduced a Semi-Supervised Classification (SSC) method incorporating a Naive Bayes (NB) classifier and Adaptive Fast Fourier Transform (AFFT). However, deep learning (DL) methods proved ineffective due to limited training samples and high dimensionality. Similarly, [24] proposed the GSSHO algorithm to enhance classification accuracy, but faced challenges due to the curse of dimensionality impacting classification accuracy. [25] introduced new deep learning models for image classification, yet encountered constraints due to the requirement of large computational resources for training. Furthermore, [26] developed a Deep Reinforcement Learning (DRL) model for band selection, but faced limitations associated with the extensive computational resources required for training RL models. Lastly, [27] introduced the 3D-HyperGAMO framework, effectively addressing class imbalance in HSI data, although traditional methods were replaced by Convolutional Neural Networks (CNNs) for classification. Despite the advancements in HSI classification methodologies, each approach faced unique limitations, underscoring the ongoing challenges in this field

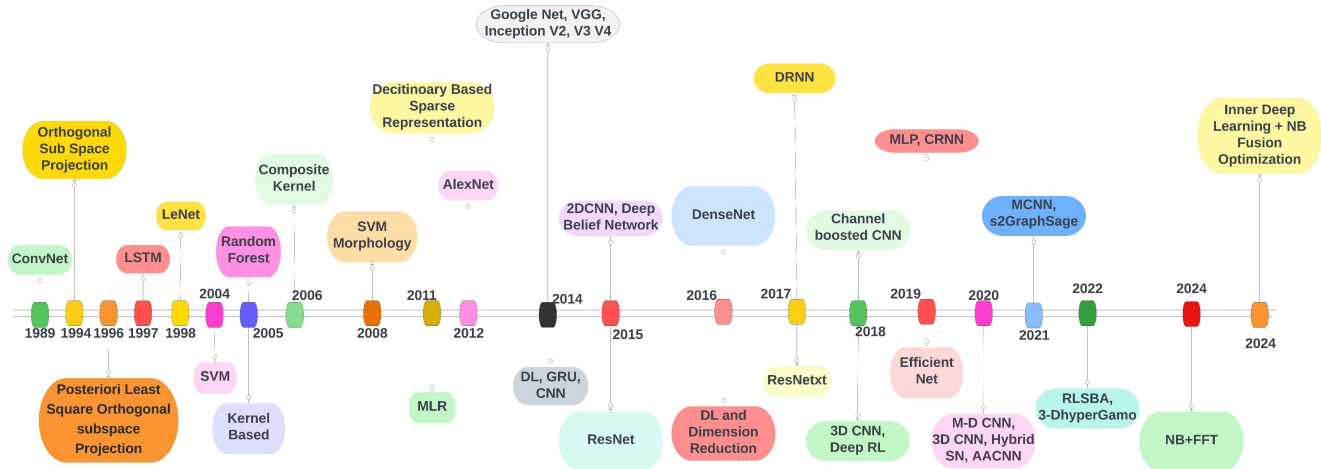


Figure 4. Most cited Research in the field of Hyper-spectral Image classification year-wise and the Evolution of CNN

and the need for further research to overcome these barriers. **Table I**, shows the comprehensive review for recent paper published on HSI.

C. Convolution Neural Network

The rise of machine learning has propelled deep learning into the global spotlight due to its remarkable accuracy and its ability to extract meaningful features from vast datasets. However, when applied to Hyperspectral Imaging (HSI), the process of learning and feature extraction becomes notably time-consuming. **Fig 4** illustrates the advancement of deep learning algorithms in the realm of HSI classification.

The journey of HSI classification in the literature commenced with a significant breakthrough in 1994 [32], introducing orthogonal subspace projection techniques. Subsequently, posterior to this milestone, the least squares orthogonal subspace projection approach was employed for HSI signature extraction and classification [33]. Throughout the first decades of the 21st century, various methods, including Long Short-Term Memory (LSTM) [34], K-Nearest Neighbors (KNN), Bayes, Decision Trees, and Random Forests, made their appearances.

Notably, Support Vector Machines (SVM) [35], kernel-based approaches [36], and Random Forests [37] gained popularity for HSI classification. However, the last 8-10 years have witnessed remarkable growth in HSI classification due to the emergence of deep learning techniques [36], [38], [39]. We meticulously selected and focused on research with significant impact and high citation counts during this period.

Some noteworthy contributions during this surge include the implementation of Logistic Regression using Machine Learning (MLR) in a cloud environment [40], dictionary-based sparse representation [41], the adoption of deep learning [42], exploration of neural translation encoder approaches such as Gated Recurrent Units (GRU) [43],

Convolutional Neural Networks (CNN) [44], [45], Deep Belief Networks [46], deep learning combined with dimension reduction [42], and the application of dictionary-based sparse representation [43].

Furthermore, techniques like Deep Recurrent Neural Networks [47], 3D deep learning frameworks [48], [49], [50], [51], Cascaded Recurrent Neural Networks [31], and Multi-Layer Perceptrons (MLP) [46] emerged as prominent contenders in HSI classification. Hybrid approaches such as Spiking Neural Networks (SNN) [52], 1D CNN [28], Morphological Convolutional Neural Networks (MCNN) [30], S2GraphSage [29], RLSBSA [26], and 3DHyperGamo [27] models have broken previous accuracy records in predicting HSI classes.

However, a limitation persists in the use of CNN, primarily designed for square images, leaving room for innovation in the extraction of crucial features from curved and edge images. In response to this, we propose a hybrid approach involving convolutional networks for HSI feature extraction and classification.

To delve into the evolution of Convolutional Neural Networks (CNN), the first CNN, known as ConvNet, was reported in 1989. It took nearly two decades to gain widespread popularity across various domains, including computer vision, image processing, object detection, video processing, natural language processing, and speech recognition. LeNet [53] made its debut in handwritten recognition, while AlexNet [54] introduced the concept of using multiple layers of convolution and pooling with Rectified Linear Unit (ReLU) activation for classifying 1000 classes.

ResNet [55] was a pivotal development, introducing skip connections and achieving impressive performance with lower time complexity. GoogleNet/Inception [56] improved upon the Inception module from LeNet and introduced a 22-layer deep convolutional neural network for image

TABLE I. Comprehensive Review

Authors	Methodology	Results	Limitations
A K Singh et al., (2024) [23]	SSC approach with NB classifier and AFFT for classification. Achieved high accuracy with IVS-SVM-AFFT-SSC method. Demonstrated generality using SVM and KNN classifiers. Novel IVS-FS method enhanced classification accuracy.	SSC method achieved highest accuracy for WDC-M dataset. NB classifier outperformed SVM and KNN. IVS-FS method significantly improved accuracy.	DL methods ineffective due to limited training samples and high dimensionality. SSC approach focuses on low training data for improved accuracy.
X Yang et al., (2023) [24]	GSSHO algorithm enhances hyperspectral image classification with chaos and optimization. Improved SHO algorithm. Initial clusters optimized with chaotic algorithms.	GSSHO algorithm excels in classification accuracy and band reduction. Shows strong global search and convergence abilities. Enhances classification efficiency.	Curse of dimensionality affects classification accuracy. Existing algorithms have shortcomings in convergence speed and search ability.
A. Hamza et al., (2023) [25]	New deep learning models for land scene image classification. Improved feature selection using controlled entropy optimization.	Architecture includes contrast enhancement, feature selection, and classification. WHU-RS19 experiment showed classification results using deep features.	Requires large computational resources for deep learning models.
J Feng et al., (2022) [26]	Deep reinforcement learning model for unsupervised hyperspectral band selection. Agent learns band-selection policy without labeled data, improving remote sensing.	Achieved highest OA using SVM classifier. Outperforms competitors when more spectral bands are chosen. Provides gains compared to other band selection models.	Requires extensive computational resources for training RL models.
S. K. Roy et al., (2022) [27]	Proposed 3D-HyperGAMO framework for minority class oversampling in HSI data. Utilized a 3-D conditional discriminator unit for classification.	Effectively handles class imbalance in HSI data. Conducted classification experiments on various datasets.	Traditional methods replaced by CNNs for HSI classification.
D. Hong et al., (2021) [28]	Investigates CNNs and GCNs for hyperspectral image classification. Introduces miniGCN for large-scale training with fusion strategies.	MiniGCNs outperform GCNs and fusion strategies enhance performance. Capture spatial relationships in HS images.	Limited scalability of GCN models to larger datasets.
P. Yang et al., (2021) [29]	Inductive learning for hyperspectral image classification with spectral graphs. Uses GraphSAGE to reduce computational complexity and enhance performance.	Outperforms state-of-the-art HSI classification methods. Achieved best performance with parameter set at 0.4.	GCN requires all nodes in training, leading to high computational cost.
SK Roy et al., (2021)[30]	MorphConvHyperNet for HSI classification, outperforming traditional CNNs. Morphological CNNs enhance feature extraction.	Outperforms baseline architecture and other methods. Superior performance in HSI classification. Investigated dilation and erosion operations with different SE sizes.	Limited interpretability of the morphological operations in the network architecture.
R Hang et al., (2019)[31]	Cascaded RNN model for hyperspectral image classification. Incorporated convolutional layers for spectral-spatial analysis.	Achieved better results than compared models. Improved overall accuracy from 86.18% to 90.30%.	Small objects in data hinder spatial feature exploration.

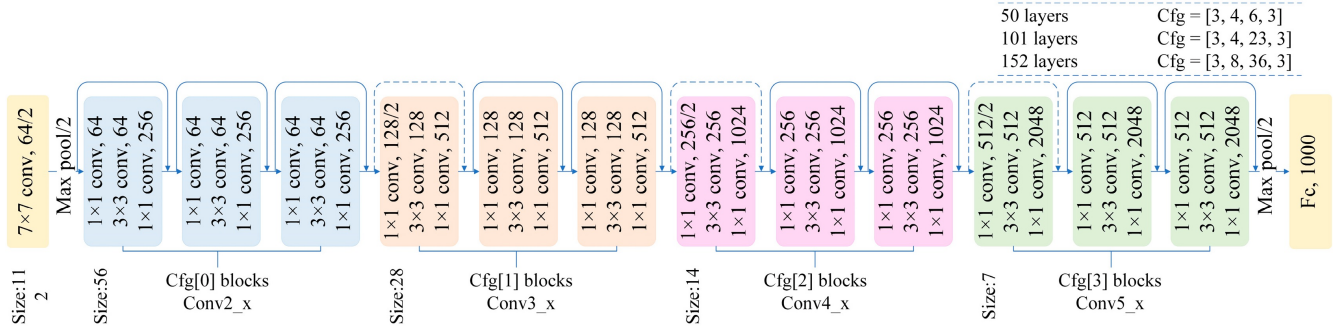


Figure 5. ResNet152 Architecture

classification. ZDNet [57] was designed to visualize network performance statistically, tracking CNN performance through neuron activation analysis.

VGG [56] conducted extensive research into denser convolutional network design, and the Inception architecture evolved rapidly with versions V1, V2, V3, and V4 [58], focusing on reducing computational complexity. DenseNet [59], [60] tackled the vanishing gradient problem by implementing cross-layer connections, similar to ResNet. Channel Boosted CNN [61] increased input channel numbers to enhance network representation capacity. RANN [62] incorporated an attention module into CNN, stacking residual blocks to identify object characteristics. The evolution of CNN, as depicted in Fig 4, showcases the consistent improvements in feature extraction and classification performance. In our research, we adopted the ResNet152 model, a widely used CNN version with proven effectiveness across various vision-related applications.

ResNet152 was named and suggested to consist of 152 layers. ResNet shows a decrease in error rate with an increase in layers. ResNet152 uses the residual blocks with skip network, thus solving gradient decent problem and enhancing network performance. Fig 5 shows the architecture of the ResNet152 model. All skip connections and layers are shown in the figure.

D. Graph convolutional network

A Graph-based convolution Network (GCN) can hold the correlated structure of HSI. It can be treated as semi-supervised learning on the graph data structure. It is capable of describing the one in non-Euclidean space. GCN architecture can preserve spectral information through localized first-order approximation. Hidden layers of GCN help encode and learn graph edges and nodes' local features. These spectral signatures of HSI are represented as an undirected graph. Let the undirected Graph is denoted as $G = (V, E)$. Where V represents vertex and E indicates edge sets, respectively. In HSI, pixels represent vertex sets, and the relation between these pixels are edges, i.e., edges represent similarities between two vertexes v_i and v_j . Let F^i denote the feature vector of the vertex v_i for S layers

can be evaluated using (1)

$$F_i^S = \beta \left(\sum_{v_j \in L(v_i)} K \left(w + H \left(\frac{F^j}{\sqrt{L(v_i) + L(v_j)}} \right) \right) \right) \quad (1)$$

Where β represents the activation function (ReLU, ELU, Tanh), $W \in \mathbb{R}$ is the weight matrix, and $L(\cdot)$ represents neighbors of a vertex. $H(\cdot)$ is a simple neural network. $K(\cdot)$ is another MLP to project the added vector into another dimension. Now to evaluate the weighted coefficient between the neighbors v_i and v_j , the edge e_{ij} is evaluated using (2)

$$e_{ij} = T \left(\frac{\exp \left(\frac{\alpha \|v_i - v_j\|^2}{\sigma^2} \right)}{\sum_{v_j \in L(v_i)} \exp((F^i, F^j))} \right) \quad (2)$$

Where σ is the parameter to control the width of the radial function, v_i and v_j are the spectral signatures associated with the pixel. α represents the empirical set [0.2, 0.8] to assign weights for distance and direction relations between adjacent regions. $T(\cdot)$ is a simple neural network. The information related to equation (2) and $N = |V| \subseteq \mathbb{R}$ as an aggregated message for all nodes can be evaluated using (3).

$$Y = e \times N \times W \quad (3)$$

Stacking in GNN will help to refine the search result and produce contextual similar features. Following Fig 6 shows the concept of GNN, where the input to GNN is the node feature $X \in \mathbb{R}^{N \times D}$, and the output is the intermediate node embedding $F^1 \in \mathbb{R}^{N \times d_1}$, where d_1 is the first embedding dimension. F^1 is made up of $F_i^1 \in \mathbb{R}^{d_1}$. F^1 is considered to be the input to the second layer, and a similar set of evolutions is done with the d_2 dimension. After a few layers, at the output of the S layer is $F^S \in \mathbb{R}^{N \times d_s}$.

E. 3D-DWT

As we know, single HS images consist of multiple narrow bands that enable the development of algorithms to extract diverse features [63]. 3D-discrete wavelet transform (3D-DWT) shown in Fig 7, can be used to decompose the image into spectral components. Later, these spectral components can be directly fed into GCN for gaining

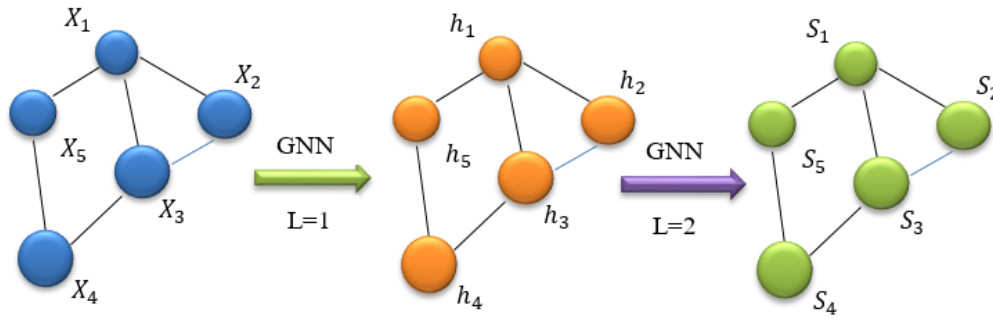


Figure 6. Layers Graph CNN

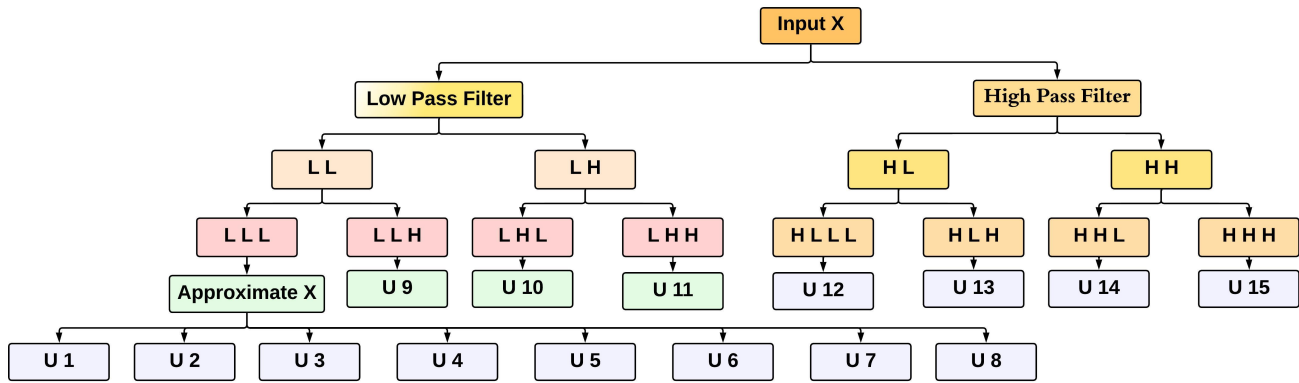


Figure 7. 3D-DWT Architecture

spectral features. Wavelet transform is mostly used in noise removal and image compression. In general, a wavelet transform (WT) can be defined as:

$$W_f(a, b) = \frac{1}{\sqrt{a}} \int_{-\infty}^{+\infty} x(t) \phi^* \left(\frac{t-b}{a} \right) dt \quad (4)$$

where a and b represent scaling and shifting parameters simultaneously used for giving frequency and time information of the input signal. $\phi(t)$ is the kernel function. DWT can be defined using:

$$W_{(p,q)}^\phi(x) = \frac{1}{\sqrt{a}} \int_{-\infty}^{+\infty} x(t) a_0^{-\frac{p}{2}} \phi \left(\frac{t-nb_0 a_0^p}{a_0^p} \right) dt \quad (5)$$

where a_0 is the scaling parameter and b_0 is the shifting parameter. Now, signal $x(t)$ can be recovered by wavelet and scaling function $\phi(t)$ and $\psi(t)$. Now, equation (5) can be rewritten for discrete signal $x(n)$ as:

$$x(n) = \frac{1}{\sqrt{M}} \sum_d C_\psi[i_0, d] \psi_{(i_0, d)}[n] + \frac{1}{\sqrt{M}} \sum_{i=i_0}^{\infty} \sum_d D_\phi[i, d] \phi_{(i_0, d)}[n] \quad (6)$$

where $x(n)$, $\psi_{(i_0, d)}[n]$, and $\phi_{(i_0, d)}[n]$ are discrete set functions. This function may vary in the range of $[0, M - 1]$ for M different points. The inner products $C_\psi[i_0, d]$ and $D_\phi[i, d]$ can

be obtained from equations (7) and (8).

$$C_\psi[i_0, d] = \frac{1}{\sqrt{M}} \sum_n x(n) \psi_{(i_0, d)}[n] \quad (7)$$

$$D_\phi[i, d] = \frac{1}{\sqrt{M}} \sum_n x(n) \phi_{(i_0, d)}[n] \quad (8)$$

In the proposed work, 3D-DWT transformation is performed using expression (5) over different 1-D DWTs. Haar wavelet is used with a different filter bank (L, H) with coefficients $l(d) = \left(\frac{1}{\sqrt{2}}, \frac{1}{\sqrt{2}} \right)$ and $h(d) = \left(1, \frac{1}{\sqrt{2}} \right)$. 3D-DWT over HS imaging is performed on each 1-D on HS hypercube. The tensor product is constructed for 3D-DWT using equations (9) and (10).

$$X^{(x,y,z)} = (L^x \oplus H^x) \otimes (L^y \oplus H^y) \otimes (L^z \oplus H^z) \quad (9)$$

$$X^{(x,y,z)} = L^x L^y L^z \oplus L^x L^y H^z \dots \oplus H^x H^y L^z \oplus H^x H^y H^z \quad (10)$$

where \oplus represents direct sum and \otimes is the product of tensor. Figure 6 shows the eight-sub band decomposition of 3D data. The sub-band can be represented using equation (11).

$$x_{(i,j)} = (U_1(i, j), (U_2(i, j)), (U_3(i, j)), \dots, (U_{15}(i, j))) \quad (11)$$

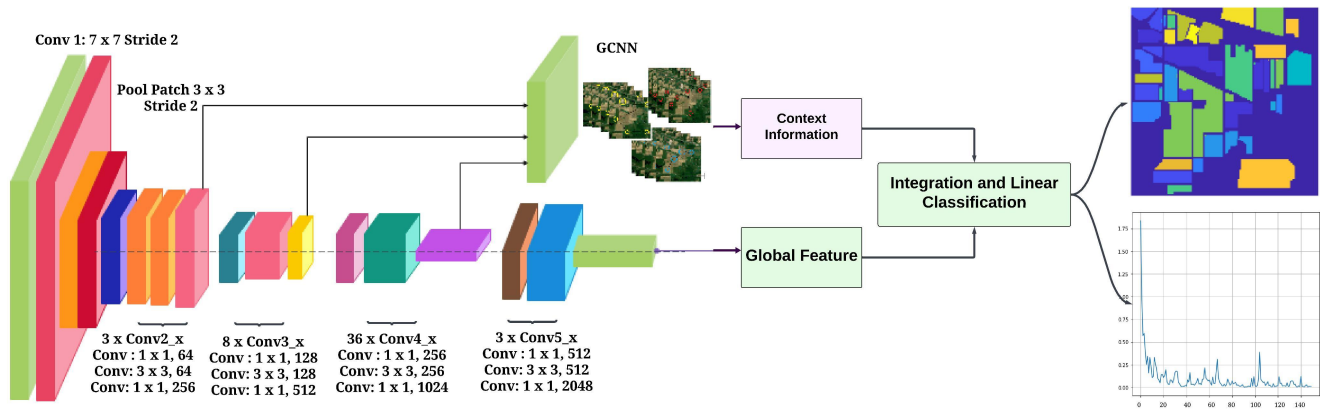


Figure 8. GCNN-RESNET152 Proposed Frame Work for HS Image

3. PROPOSED ARCHITECTURE: HYBRID CONVOLUTION NETWORK

HSI contains process information from the electromagnetic spectrum. HS Image is in the form of a hypercube where each pixel spectrum of a narrow wavelength band is stored in 3D space. The spatial information is held over the x and y axis, whereas spectral information is stored on the z -axis. The image is in the form of a 3D (x, y, λ) . HSI image analysis is processing the hypercube and extracting local and global features. The exploration of spectral bands from global visual features and local contextual information can be the solution to perfectly identifying the patches in HSI images with overlapping boundaries and edges. In this view, we propose a Hybrid Convolution Network to explore the discriminative ability of the pre-trained ResNet152 model. As shown in **Fig 8**, the GCNN-RESNET152 consists of two synthesized; the spectral band global features and local contextual as FC features. In **Fig 8**, we provide a visual representation of our proposed GCNN-RESNET152 model. This Fig illustrates how the spectral band global features and local contextual features are synthesized within the network. By doing so, we aim to improve the accuracy of identifying patches in HSI images, especially those with complex overlapping boundaries and edges. This innovative approach has the potential to advance various applications reliant on HSI data, offering more precise material and object identification.

The novelty of our work lies in its approach of combining deep learning, particularly GCNNs-RESNET152, with HSI to address longstanding challenges in feature extraction and classification. Our innovative hybrid model, which combines elements of both CNN and GCN, addresses some of the limitations associated with traditional CNN models. By leveraging global and context features effectively, we achieve remarkable classification results, particularly with the Extreme Machine Learning classifier, surpassing the performance of other cutting-edge algorithms on benchmark datasets. This demonstrates the promise of our approach in advancing hyperspectral image classification and its potential applications in various domains. This innovative

approach has the potential to enhance the accuracy and applicability of HSI across a range of domains, ultimately contributing to more informed decision-making and discoveries Authors and Affiliations.

4. RESULT ANALYSIS

A. Data Description

For quantitative and qualitative evolution of proposed model experiments is conducted over four benchmark datasets.

- 1) The Indian Pines (IP) Dataset was obtained using the Airborne Visible/Infrared Imaging Spectrometer (AVIRIS) from a ground distance of 20 meters. It comprises 220 spectral bands and has an image size of 145x145 pixels, with a spectral resolution of 10nm. This dataset encompasses 16 distinct land-cover categories. For our analysis, we divided the dataset into 695 samples for training and 9671 samples for testing, and additional details can be found in **Table II**.
- 2) The Pavia University (PU) Dataset was collected using the Reflective Optics System Imaging Spectrometer (ROSIS) sensor. It consists of an image with dimensions 610x340 pixels and encompasses 103 spectral bands spanning the range from 430nm to 860nm. This dataset is categorized into 9 different land-cover classes, and additional details can be found in **Table III**.
- 3) The Houston2013 (HU) dataset was captured using the ITRES CASI-1500 sensor. It features an image size of 349x1905 pixels with a spectral resolution of 10nm. The dataset comprises 144 spectral bands spanning the range from 364nm to 1046nm. Detailed information regarding the land-cover categories within the Houston dataset, which total 15, is provided in **Table IV**.
- 4) The Kennedy Space Center (KSC) dataset was acquired using an AVIRIS sensor, covering a wide wavelength range from 400nm to 2500nm. The im-

age has dimensions of 512x614 pixels and includes 176 spectral bands. This dataset encompasses 13 distinct categories related to wetlands, totaling 5202 labeled samples, as outlined in **Table V**.

B. Experimental Setup

ResNet152 is implemented using the Tensor Flow platform, and Adam [64] is used for optimization. The current learning rate is dynamically updated by multiplying the base learning rate by 0.5 at an interval of every 10 epochs. The maximum number of epochs is set to 100. Batch-wise normalization [65] is used with a momentum of 0.6 and batch size 64. Training of the network is done with 10-fold cross-validation. The accuracy of the result is measured using indices Overall Accuracy (OA), Average Accuracy (AA), and Kappa Coefficient (κ).

C. Multilayer Feature Extraction

ResNet152 is a deep learning model comprising convolutional, pooling, activation, and fully connected (FC) layers. During feature extraction, the FC layer, although losing some spatial information, serves as a global representation for classification purposes. ResNet152 is structured with four convolution layers, namely convs2_x, conv3_x, conv4_x, and conv5_x, each with different dimensional sizes (256, 512, 1024, and 2048 real numbers).

To capture the spectral structure of Hyperspectral Imaging (HSI) images effectively, we employ a graph-based convolutional network. Additionally, we utilize a 3D wavelet transform over the HSI hypercube, preserving both spatial and spectral information. The coefficients obtained from the 3D-DWT process are extracted at multiple levels. Specifically, the LLL sub-bands capture spatial information in the second-level 3D-DWT, while the LLH band retains spectral information from the HSI data. These sub-band knowledge representations are concatenated, resulting in a 3D data cube correlation. In **Fig 9**, we illustrate the output of the 3D-DWT approximation and detail levels from 1 to 3, covering slices 1 to 25. This Fig provides a visual representation of the 3D-DWT wavelet decomposition, utilizing a near-symmetric wavelet. Furthermore, in **Fig 10**, we demonstrate the refinement of convolutional features transformed by the 3D-DWT, showing the impact of our proposed Graph Convolutional Neural Network (GCNN) on the HSI data. This refinement step enhances the effectiveness of feature extraction and classification within the HSI dataset.

D. Feature Fusion

Since the proposed approach uses two deep learning approaches for feature extraction, an effective fusion strategy is required to fuse to obtain discriminative features. FC_GCNN treated contextual information, and FC_ResNet152 held global information. The weighted concatenation method is adopted for integration for the proposed Hybrid DWT-based GCNN and ResNet152 model. The final feature can be acquired using (12).

$$F_{final} = [F_{GCNN}, \gamma FC_{ResNet152}] \quad (12)$$

Now, F_{final} can be used for training and testing a linear classifier.

E. Experiment Analysis

The proposed method's performance is evaluated using indices OA, AA, and κ . OA is the percentage of the number of samples correctly classified N_C over the available sample N_A . AA is the average of classification accuracy for all class levels, and Kappa coefficient (κ) is the ratio between producer's accuracy for the classification result.

$$OA = \frac{N_C}{N_A} \times 100\% \quad (13)$$

$$AA = \frac{1}{Cl} \sum_{m=1}^{Cl} \frac{N_C^m}{N_{All}^m} \times 100\% \quad (14)$$

$$\kappa = \frac{OA - P_e}{1 - P_e} \times 100\% \quad (15)$$

The final integrated features F_{final} is fed into a set of linear classification SVM, KNN, DT, Naïve Bayes, and extreme machine learning EML. **Fig 11** compares each classifier's accuracy over OA, AA, and kappa. It can be seen that the performance of EML is better than other classifiers. The OA accuracy achieved by EML is 94.4 ± 1.30 , 92.31 ± 1.78 , 97.48 ± 2.15 , and 97.7 ± 0.58 for four datasets IP, HU, KSC, and PU dataset, which is 3 to 5% better than OA achieved using SVM, NB, KNN, and DT. Similar performance is measured for AA and kappa accuracy for all the five classifiers, and EML has better than the rest. Since the performance of the model solely depends upon the quality of matrix e_{ij} (eq. 2), which is influenced by two parameters: the number of neighbor κ and σ as the width of the radial function. We have shown the changing trends in two parameters and their contribution. **Fig 12** shows the OA achieved through the different combinations of these two parameters. Tables VI-IX quantitatively report the classification scores obtained by different methods in terms of OA, AA, and κ , as well as the individual class accuracy's for the Indian Pines, Pavia University, and Houston2013 datasets, respectively. Comparison is only listed with the state-of-the-art methods, which they claimed to be superior in comparison to traditional classifiers. Hence, we have not tested our model with a traditional classifier. The comparison is made with random forest [37], MLR [40], SVM [35], MLP [66], RNN [31], LSTM [48], GRU [48], CNN-1D [28], CNN-2D [44], CNN-3D [50], MorphCNN [30], RLSBSA [26], 3DHyperGamo [27] and S2GraphSage [29]. The obtained accuracies for disjoint training and test samples are shown in Tables VI-IX and **Fig 13, 14, 15, and 16**. For the dataset Pavia University, the result of the proposed methodology shows the highest overall average and kappa accuracies which are 94.4%, 96.6%, and 93.2%, respectively. Similarly, the test accuracy on the KSC dataset achieved is 97.48%, 99.68%, and 96.43% overall, average kappa accuracy. The test result for the other two datasets is also superior to state-of-art algorithms. An effort is made to show the visual comparison (**Fig 13-16**)



TABLE II. INDIAN PINES DATASET LAND COVER 16 CATEGORIES DISTRIBUTED OVER TRAINING AND TESTING SAMPLES.

Category	Training Testing
Corn Notil	50, 1384
Corn Mintil	50-784
Corn	50-184
Grass Pasture	50-447
Grass Trees	50-697
Hay Windrowed	50-439
Soybean Notil	50-918
Soybean Mintill	50-2418
Soybean Clean	50-564
Wheat	50-162
Woods	50-1244
Buildings Grass Trees Drives	50-330
Stone Steel Towers	50-45
Alfalfa	15-39
Grass Pasture Mowed	45611
Oats	45427
Total	695-9671

TABLE IV. HOUSTON2013 DATASET LAND COVER 15 CATEGORIES DISTRIBUTED OVER TRAINING AND TESTING SAMPLES.

Category	Training Testing
Healthy Grass	198-1053
Stressed Grass	190-1064
Synthetic Grass	192-505
Tree	188-1056
Soil	186-1056
Water	182-143
Residential	196-1072
Commercial	191-1053
Road	193-1059
Highway	191-1036
Railway	181-1054
Parking Lot1	192-1041
Parking Lot2	184-285
Tennis Court	181-247
Running Track	187-473
Total	2832-12197

between ResNet152 and the proposed model in the form of classification maps. In general, ResNet152 pixel-wise classification models result in noise in the classification maps. The proposed approach of using discrete wavelet transform and implementing GCNN for batch-wise feature fused with ResNet152 elements can preserve global and local information, thus resulting in better visibility and classification accuracy.

5. NOVELTY & SUMMARIZATION

The novelty of our work lies in the development and application of a hybrid feature extraction and classification

TABLE III. PAVIA UNIVERSITY DATASET LAND COVER 9 CATEGORIES DISTRIBUTED OVER TRAINING AND TESTING SAMPLES.

Category	Training Testing
Asphalt	584-6304
Meadows	540-18146
Gravel	392-1815
Trees	524-2912
Metal Sheets	265-1113
Bare Soil	532-4572
Bitumen	375-981
Bricks	514-3364
Shadows	231-795
Total	3921-40002

TABLE V. KENNEDY SPACE CENTRE DATASET LAND COVER 13 CATEGORIES DISTRIBUTED OVER TRAINING AND TESTING SAMPLES.

Category	Training Testing
CP Hammock	25-231
Hardwood	22-207
Spartina Marsh	50-470
Mud Flats	50-453
Scrub	70-691
Slash Pine	25-227
Swap	20-85
Cattail Marsh	40-364
Water	90-837
Willow Swamp	25-218
Oak / Broadleaf	20-141
Graminoid Marsh	40-391
Salt Marsh	40-379
Total	517-4694

model, GCNN-RESNET152, for hyperspectral image (HSI) classification. This approach combines the strengths of two distinct techniques, ResNet152 and Graph Convolutional Network (GCN), to achieve superior results in HSI classification.

- Global Feature Extraction with ResNet152: Our work begins by employing the ResNet152 model, a well-established deep learning architecture, for global feature extraction from hyperspectral images. While ResNet models are commonly used in image classification tasks, their application in hyperspectral



TABLE VI. Indian Pine quantitative comparison in terms of OA, AA, AND κ with state-of-art algorithms.

Class	RF	MLR	SVM	MLP	RNN	LSTM	GRU	CNN-1D	CNN-2D	CNN-3D	Hybrid SN	Morph CNN	RLSB S-A	3D-HG	s2G SAGE	Proposed GCNN-RESNET152
1	85.33	80	88	73.6	58.4	89.6.0	77.6	80.8	73.64	48.18	82.66	92.27	91.3	70	100	100
2	55.11	81.48	80	81.45	75.5	82.22	81.1	79.38	83.12	85.12	82.17	84.05	97.8	33.33	74.21	98.8
3	22.77	54.11	69.55	64.55	63.37	64.16	70.35	74.26	81.98	77.22	76.73	79.34	97.3	97.33	88.28	98.60
4	13.13	38.38	48.48	47.07	29.49	55.35	53.33	31.92	45.39	50.11	33.33	52.14	95.4	74.24	96.18	98.25
5	41.6	91.97	87.23	86.94	87.59	89.27	88.4	90.73	89.11	80.28	81.14	91.66	94.7	96.67	94.45	96.21
6	94.06	94.63	96.33	95.93	95.31	96.39	96.38	96.39	95.02	89.81	97.36	95.74	98.7	37.71	98.39	99.20
7	0	0	50	10.02	0	0	0	0	0	0	0	0	93.3	76.16	100	95.60
8	91.33	100	100	99.84	99.52	99.2	99.12	99.84	99.96	95.96	96.53	100	100	98.53	99.69	100
9	40	0	50	80	56	76	66	50	26.66	77.78	66.66	44.44	100	62.29	100	100
10	26.83	66.76	76.54	75.35	71.13	81.51	78.53	81.83	77.44	77.9	74.35	80.77	95	86.29	90.18	97.20
11	81.06	84.13	87.7	83.19	78.86	80.4	82.29	80.39	89.4	82.73	79.18	88.54	99	96.52	80.32	100
12	28.95	66.31	77.3	78.58	71.91	76.31	83.19	84.75	87.72	82.64	71.04	88.46	97.6	61.63	93.49	100
13	86.25	95	97.5	98	97	97.25	97.75	97.75	95.28	89.72	96.25	87.64	100	89.13	98.12	100
14	91.07	90.64	91.38	92.92	90.28	94.13	92.88	93.32	98.94	98.31	91.68	98.82	99.1	98.23	94.35	100
15	10.1	89.9	80.81	87.88	75.56	90.71	93.54	89.9	82.02	55.17	45.45	69.44	99.6	89.48	88.07	100
16	71.96	97.73	97.73	87.27	88.64	94.09	95.45	96.82	82	82.5	84.09	84	91.6	91.92	98.61	97.62
OA	60.8	80.33	84.12	82.95	79.07	83.55	84.2	84	87.25	83.6	80.86	87.45	97.9	86.96	87.43	99.86
AA	52.47	70.69	79.91	77.66	71.16	79.16	78.49	76.76	75.48	73.34	72.41	77.33	96.9	78.82	93.4	98.84
$\kappa(x100)$	54.41	77.47	81.87	80.56	76.12	81.27	82.01	81.81	85.48	81.36	78.24	85.75	97.6	85.17	85.66	99.56

TABLE VII. Kennedy Space centre (KSC) quantitative comparison in terms of OA, AA, AND κ with state-of-art algorithms.

Class	RF	MLR	SVM	MLP	RNN	LSTM	GRU	CNN-1D	CNN-2D	CNN-3D	Hybrid SN	Morph CNN	3D-HG	s2G SAGE	Proposed GCNN-RESNET152
1	99.69	100	94.13	99.18	87.33	92.22	89.44	99.79	85.52	97.17	100	97.63	97.33	99.7	100
2	98.38	99.03	0.0±0	86.63	63.12	81.64	70.85	99.19	67.31	92.91	100	86.79	71.68	98.99	100
3	99.23	99.54	54.59	84.25	69.72	75.38	78.89	95.11	60.09	81.04	99.69	98.31	88.84	99.37	100
4	88.16	99.06	17.28	78.97	47.82	58.09	44.08	77.73	45.17	44.54	99.53	88.94	89.9	78.26	100
5	73.72	100	0	13.38	68.37	74.21	65.21	80.53	67.4	85.15	98.78	48.66	82.99	83.05	99.28
6	88.88	100	0	78.12	56.24	65.12	59.82	91.97	65.47	62.74	100	86.32	77.82	80.8	100
7	100	89.88	0	78.65	83.52	90.26	89.14	95.13	77.15	80.52	97.75	97.75	99.74	99.44	98.32
8	85.51	100	60.1	89.62	65.57	71.4	69.76	97.45	64.75	71.49	99.9	70.76	99.58	98.53	100
9	96.68	100	89.37	97.59	88.39	90.72	86.72	99.92	89.22	98.94	100	91.93	94.95	100	100
10	99.22	100	98.83	96.5	92.42	88.92	88.53	99.9	73.08	90.67	100	100	99.37	96.56	100
11	100	98.03	94.94	98.5	83.89	90.26	84.83	100	87.55	97.56	96.34	100	98.85	99.64	98.33
12	97.89	99.29	89.25	98.52	81.31	87.46	83.57	98.36	82.48	99.3	99.06	97.89	98.3	94.83	100
13	100	100	100	100	99.88	100	99.92	100	99.92	100	100	100	100	99.43	100
OA	96.17	99.45	72.84	91.76	81.47	86.1	82.76	97.18	79.98	89.71	99.48	92.76	95.31	99.67	99.85
AA	94.41	98.83	53.73	84.61	75.96	81.97	77.75	95	74.24	84.77	99.31	89.61	92.26	94.51	99.68
$\kappa(x100)$	95.74	99.4	69.29	90.82	79.33	84.51	80.79	96.86	77.63	88.51	99.43	91.94	94.78	96.27	99.8

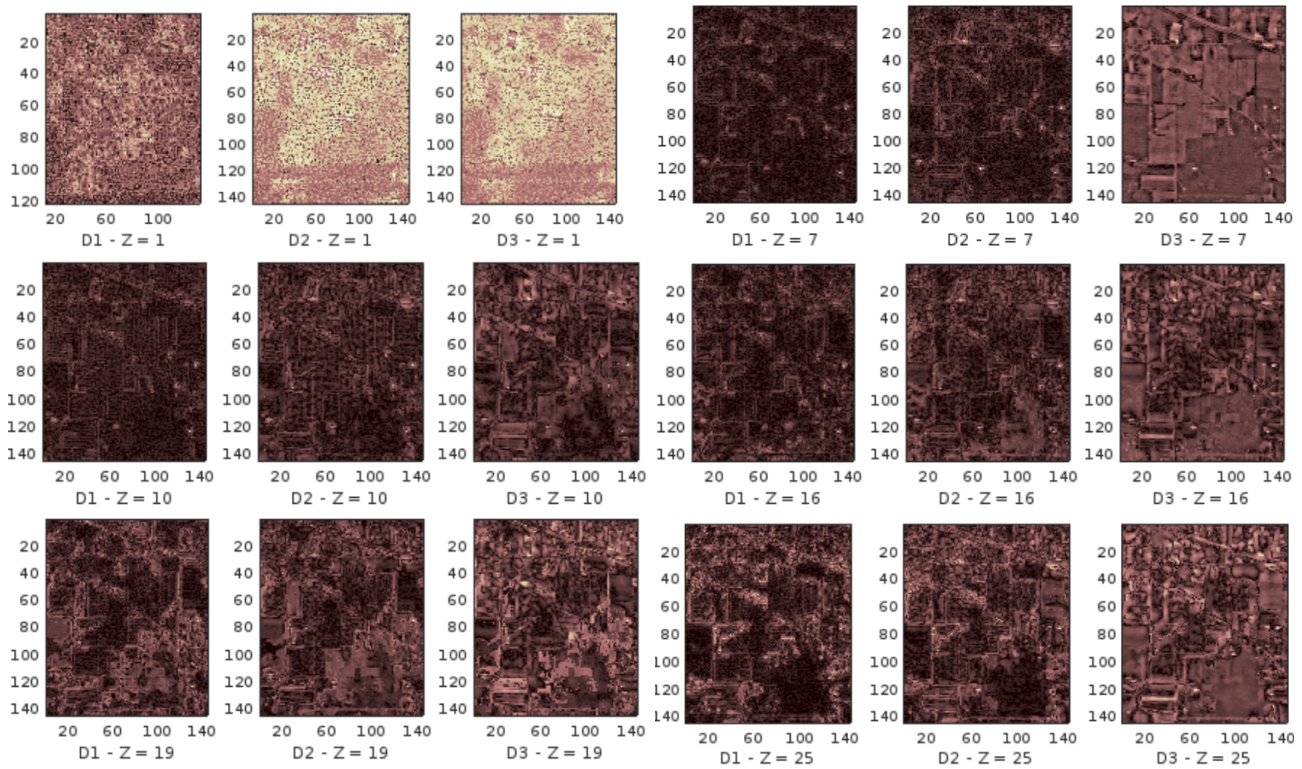


Figure 9. 3D-DWT approximation and details at level 1 to 3 for slice 1 to 25 for the Indian pine dataset

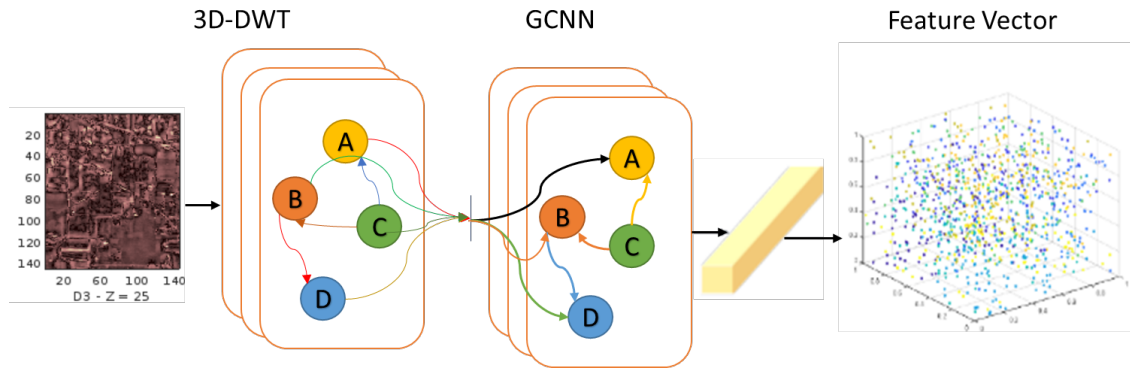


Figure 10. Refining of 3D-DWT transformed convolution feature by GCNN

imagery is relatively novel. This initial step allows our model to capture high-level information from the HSI data, which is crucial for accurate classification. By adapting ResNet152 for this specific domain, we bring a fresh perspective to hyperspectral image analysis.

- Context Feature Extraction with GCN: The second unique aspect of our work involves the use of the Graph Convolutional Network (GCN) to extract context features from the 3D discrete wavelet transform image. GCN is typically employed in graph-based data, and its application to hyperspectral imagery is

a novel and innovative approach. By doing so, we enable our model to capture intricate topological and geometric features present in geospatial images. This capability is essential for precise classification, especially in scenarios where the spatial context plays a critical role. The adaptation of GCN for hyperspectral image analysis represents a significant advancement in the field.

- Integration of Extracted Features: The integration of both global features from ResNet152 and context features from GCN using weighted methods is another novel aspect of our work. This fusion of

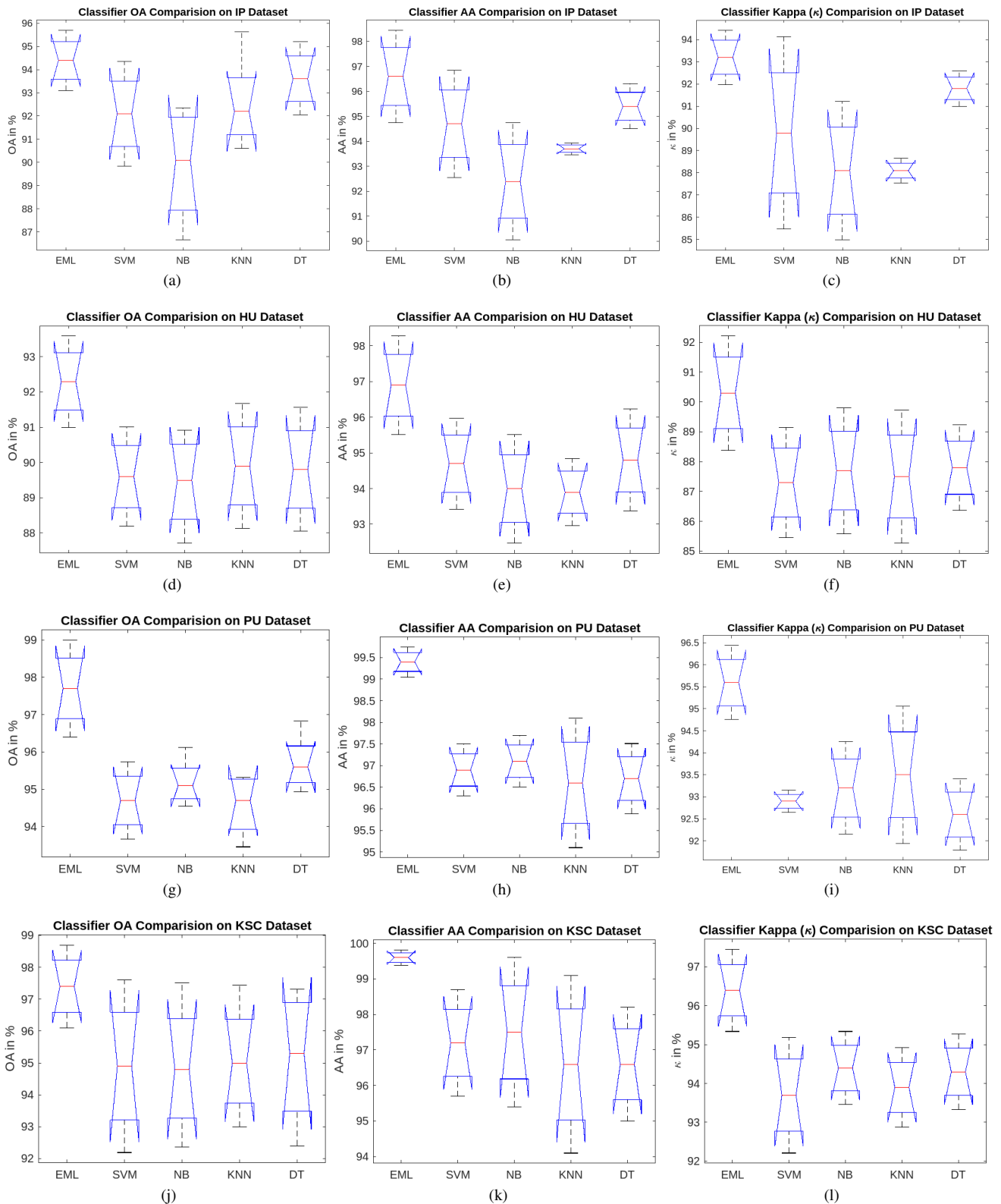


Figure 11. Accuracy Comparison in terms of OA, AA and κ in % with EML, SVM, Naïve Bayes, KNN and DT classifier for all the four dataset (a-c)IP dataset (d-f) HU dataset (g-i) PU dataset (j-l) KSC dataset

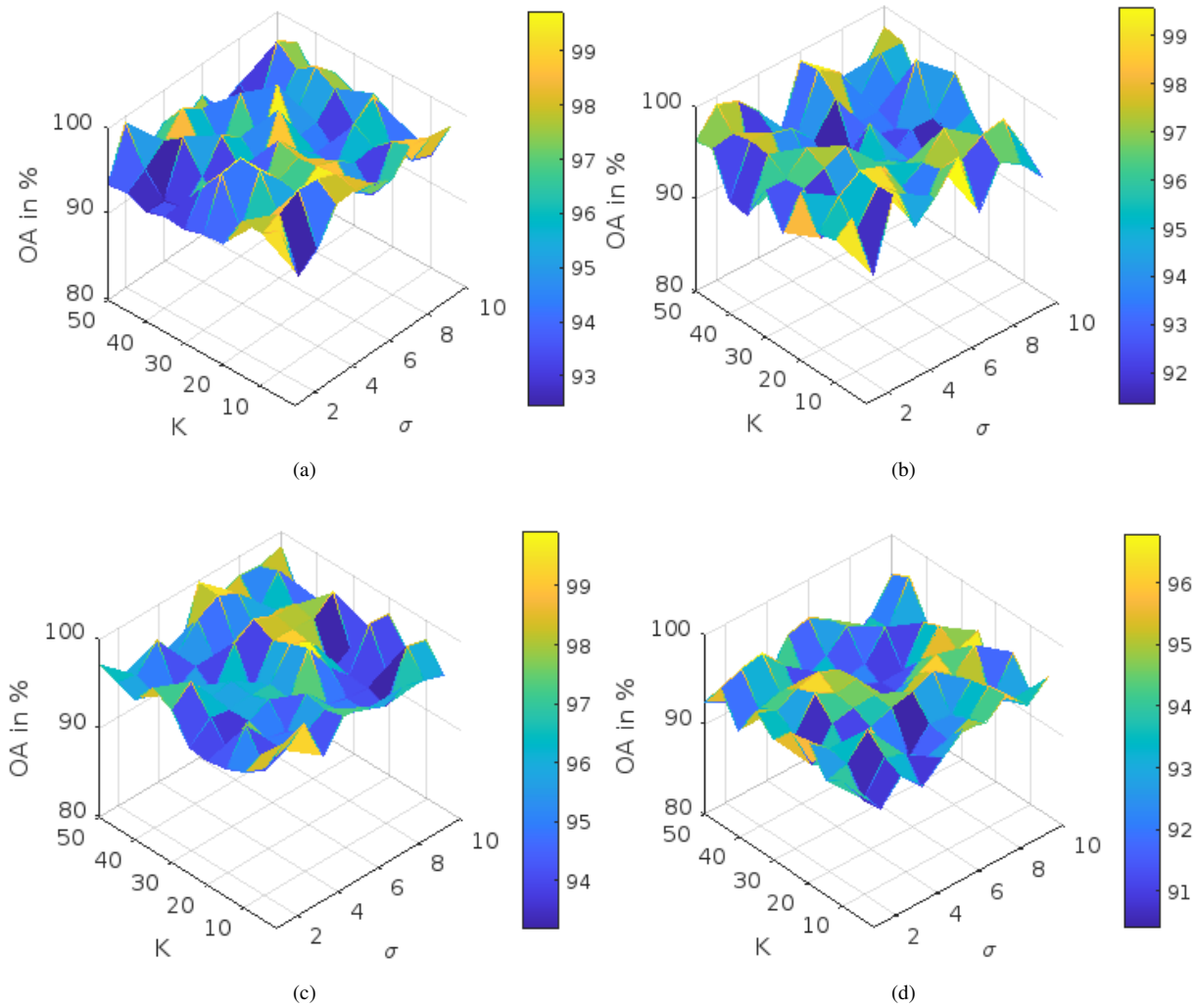


Figure 12. Parameter analysis of σ and κ for OA on datasets a) IP b) KSC c) PU, and d) HU

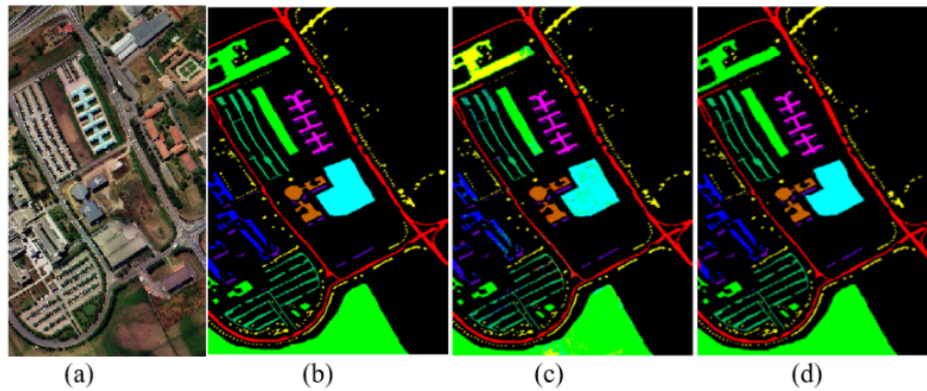


Figure 13. Classification Map on Pavia University dataset a) Original RGB Image b) Ground Truth c) ResNet152 d) Proposed hybrid GCNN-RESNET152

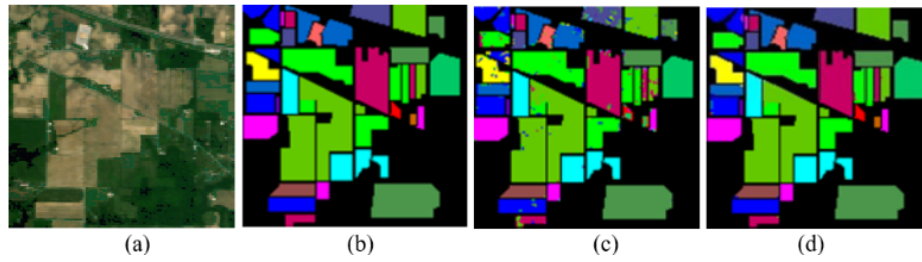


Figure 14. Classification Map on Indian Pine dataset a) Original RGB Image b) Ground Truth c) ResNet152 d) Proposed hybrid GCNN-RESNET152

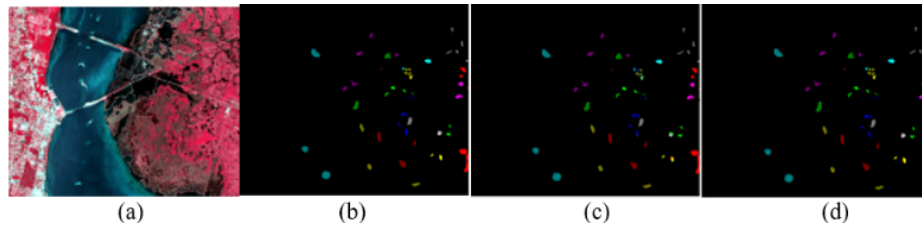


Figure 15. Classification Map on KSC dataset a) Original RGB Image b) Ground Truth c) ResNet152 d) Proposed hybrid GCNN-RESNET152

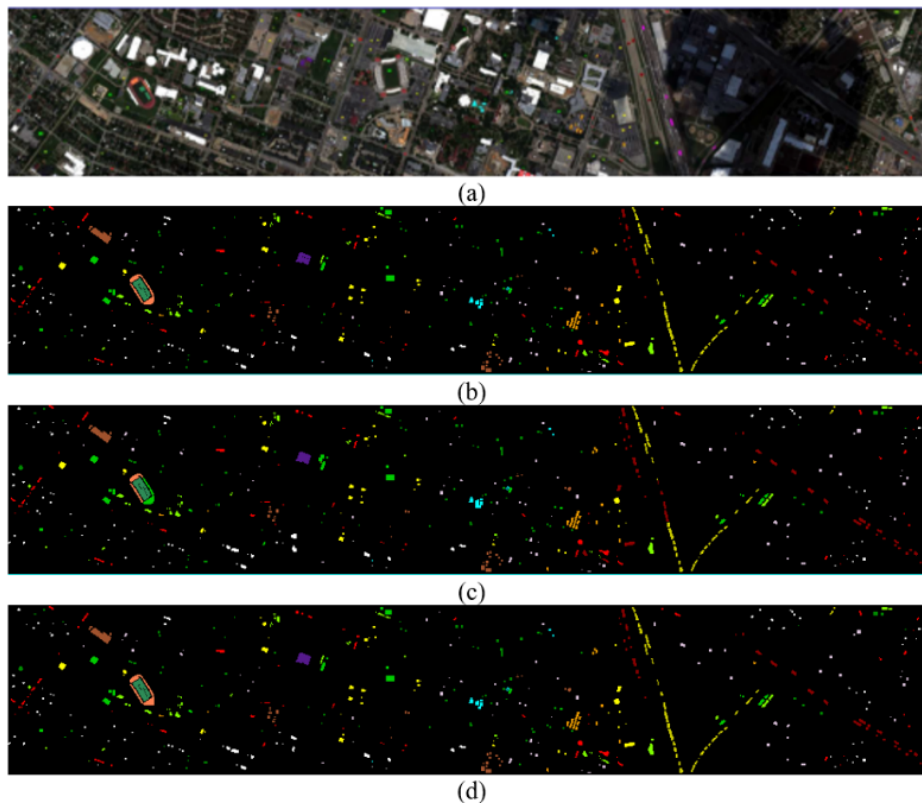


Figure 16. Classification Map on Houston dataset a) Original RGB Image b) Ground Truth c) ResNet152 d) Proposed hybrid GCNN-RESNET152

TABLE VIII. Pavia University quantitative comparison in terms of OA, AA, AND κ with state-of-art algorithms.

Class	RF	MLR	SVM	MLP	RNN	LSTM	GRU	CNN-1D	CNN-2D	CNN-3D	Hybrid SN	Morph CNN	RLSB S-A	3D-HG	s2G SAGE	Proposed GCNN-RESNET152
1	89.98	77.68	82.23	84.53	83.08	82.63	77.25	87.18	93.4±	85.66	89.74	94.52	99.8	97.4	84.87	99.9
2	74.39	58.79	65.81	75.13	67.9	78.74	80.1	89.64	96.84	95.88	81.78	97.12	99.9	99.49	95.29	100
3	38.42	67.21	66.72	68.37	65.17	60.73	54.79	71.1	65.48	68.11	82.88	85.08	98.6	91.71	85.96	98.6
4	98.24	74.27	97.77	93.5	90.72	97.1	92.05	95.32	95.55	97.02	83.66	97	99.4	71.31	83.63	100
5	95.98	98.88	99.37	99.37	99.23	99.28	99.51	99.48	98.03	98.9	99.94	99.25	99.9	98.3	99.52	100
6	51.43	93.53	91.62	89.94	85.07	65.94	74.86	88.28	80.52	68.85	72.43	93.92	100	97.99	85.85	100
7	80.63	85.08	87.36	87.2	82.94	84.95	90.17	86.77	89.29	73.09	96.16	84.98	98.4	97.25	96.78	98.4
8	97.64	87.58	90.46	90.37	85.85	88.89	90.42	90.43	94.5	95.21	92.8	96.62	99.5	94.1	94.16	100
9	94.92	99.22	93.71	98.44	94.52	98.29	93.51	97.33	95.8	93.54	94.04	97.05	99.3	92.09	97.67	100
OA	77.44	72.23	77.8	82.05	77.07	80.38	80.7	89.09	92.55	89.43	84.18	95.51	99.7	93.9	91.41	99.95
AA	80.18	82.47	86.12	87.43	83.83	84.06	83.63	89.5	89.94	86.25	88.16	93.95	99.4	93.29	91.53	99.65
$\kappa(x100)$	70.44	65.44	72.06	76.89	70.84	74.32	74.76	85.5	89.9	85.61	79.13	93.95	99.6	91.86	88.61	99.7

TABLE IX. Houston University quantitative comparison in terms of OA, AA, AND κ with state-of-art algorithms.

Class	RF	MLR	SVM	MLP	RNN	LSTM	GRU	CNN-1D	CNN-2D	CNN-3D	Hybrid SN	Morph CNN	RLSB S-A	3D-HG	s2G SAGE	Proposed GCNN-RESNET152
1	82.87	82.24	82.34	81.23	82.22	82.76	82.58	82.28	82.25	82.1	82.74	82.43	94.22	82.87	82.24	95.6
2	82.51	82.5	83.36	82.29	82.87	80.19	81.64	91.78	84.15	84.14	90.91	84.42	97.23	82.51	82.5	98.6
3	64.09	99.8	99.8	99.72	99.72	99.68	99.88	99.92	90.31	77.85	98.81	97.21	60.22	64.09	99.8	98.4
4	92.04	98.3	99.96	87.58	93.5	91.23	93.22	94.36	87.24	89.24	83.96	92.37	93.86	92.04	98.3	99.9
5	99.81	97.44	99.77	97.35	97.76	97.65	97.37	98.77	99.51	98.97	99.46	99.77	100	99.81	97.44	100
6	96.27	94.11	97.9	94.55	95.1	97.06	98.32	95.8	96.43	98.91	98.60	99.16	90.20	96.27	94.11	97.9
7	86.19	73.37	77.43	75.24	81.41	78.88	77.03	82.78	86.44	85.48	75.62	88.07	95.57	86.19	73.37	97.6
8	41.69	63.82	60.3	57	40.06	40.11	53.62	75.51	70.03	62.06	93.16	72.09	98.46	41.69	63.82	99.4
9	86.02	70.23	76.77	75.9	76.54	81.55	79.06	81.44	79.53	80.81	81.39	84.09	92.45	86.02	70.23	94.7
10	36	55.6	61.29	48.78	47.44	47.37	49.54	68.71	60.22	54.75	76.51	62.86	96.21	36	55.6	98.9
11	64.67	74.21	80.55	76.25	76.24	76.38	80.82	85.24	82.93	66.78	89.21	89.15	94.34	64.67	74.21	95.8
12	67.27	70.41	79.92	75.31	76.33	79.98	84.15	89.93	92.87	93.83	96.28	93.02	97.38	67.27	70.41	98.6
13	89.23	67.72	70.88	73.18	69.12	71.37	72.63	74.88	86.21	82.34	86.78	89.61	95.25	89.23	67.72	98.4
14	100	98.79	100	99.84	100	99.11	99.92	99.68	98.92	96.31	100	99.19	100	100	98.79	100
15	90.06	95.56	96.41	97.8	97.59	98.14	98.22	98.48	77.63	75.85	100	97.04	100	90.06	95.56	100
OA	75.38	78.97	81.86	78.22	77.95	78.16	80.21	86.42	83.27	80.24	88.31	86.51	92.31	75.38	78.97	93.59
AA	78.58	81.63	84.31	81.45	81.06	81.43	83.2	87.97	84.98	81.96	90.23	88.78	96.9	78.58	81.63	98.25
$\kappa(x100)$	73.49	77.3	80.43	76.55	76.23	76.52	78.66	85.27	81.89	78.62	87.33	85.4	90.33	73.49	77.3	91.59

information is a key innovation, as it allows our model to leverage the strengths of both feature extraction processes. By combining these features, we enhance the model's overall classification performance. This integrated approach to feature extraction and fusion represents a unique contribution to the HSI classification literature.

- Classification with Various Linear Classifiers: In our work, we explore various linear classifiers, including Support Vector Machine, Decision Tree, Naïve Bayes, K-Nearest Neighbors (KNN), and Extreme Machine Learning (EM), for the classification task. While these classifiers are not novel in themselves,

our application of them within the context of our hybrid feature extraction framework is innovative. We systematically evaluate these classifiers to determine their effectiveness in utilizing the integrated features from our model.

- Superior Performance of Extreme Machine Learning (EML): One of the most striking findings from our experiments is the consistent outperformance of the Extreme Machine Learning (EML) classifier in terms of classification accuracy. This result underscores the effectiveness of our proposed hybrid model in providing discriminative features for accurate HSI classification. The preference for EM among a range



of classifiers highlights a unique and powerful aspect of our approach.

In summary, our work introduces several novel elements to the field of hyperspectral image classification. From the adaptation of ResNet152 and GCN for feature extraction to the integration of these features and the preference for Extreme Machine Learning as the classifier, each component contributes to the innovation of our approach. Our research not only advances the state-of-the-art in HSI classification but also offers new perspectives and methodologies that can potentially benefit other image analysis domains. The combination of these novel elements makes our work a significant contribution to the field of hyperspectral image analysis.

6. CONCLUSIONS AND FUTURE WORK

To preserve the context information of the pixels, the graph structure can characterize the HS image data structure in 3D space. The noise can be filtered using 3D-DWT for retrieving smoothing features. The HS Image is trained in batches, thus achieving flexible lower computational cost. Our approach of combining the global and contextual features uses GCNN and ResNet152 to reach diverse and discriminative features representation of HSI. These Features are classified using a different set of classifiers. Accuracy archived of Extreme machine learning has reported maximum accuracy in terms of overall, average, and kappa accuracy. We have used the weighted concatenation method adopted for the integration of features. Our experiment is conducted on four different HSI datasets. The result successfully proves the superiority of the proposed model over all other state-of-art algorithms.

In the future, we would like investigate different possible combinations with an advanced fusion strategy to exploit the spectral information of HSI. The success of deep learning models often relies on meticulous hyper parameter tuning, including learning rates, batch sizes, and architectural choices. Failing to find the optimal set of hyper parameters can lead to suboptimal performance. In future work will also focus on designing optimization techniques for parameter tuning. Some other limitation is data dependency, where model's performance is highly dependent on the quality and representativeness of the training dataset. It may not generalize well to new or unseen datasets, which is a common challenge in machine learning. To come over this we would like to check model performance over another dataset also.

ACKNOWLEDGEMENT

The work is carried out under the guidance of Dr. Kailash Shaw(KS), and Dr. Minakhi Rout(MR) by Mr. Rahul Ghotekar (RG). The research, coding, testing, and documentation is done by RG. Research direction, validation, cross examining, and Documentation proof reading are done by KS and MR.

REFERENCES

- [1] R. Gogineni and A. Chaturvedi, "Hyperspectral image classification," in *Processing and Analysis of Hyperspectral Data*. London United Kingdom: IntechOpen, 2019.
- [2] L. Zhang and B. Du, "Deep learning for remote sensing data: A technical tutorial on the state of the art," *IEEE Geosci. Remote Sens. Mag.*, vol. 4(2), p. 22–40, 2016.
- [3] E. Blanzieri and F. Melgani, "Nearest neighbor classification of remote sensing images with the maximal margin principle," *IEEE Trans. Geosci. Remote Sens.*, vol. 46(6), p. 1804–1811, 2008.
- [4] Y. Tarabalka, M. Fauvel, J. Chanussot, and J. A. Benediktsson, "Svm-and mrf-based method for accurate classification of hyperspectral images," *IEEE Geosci. Remote Sens. Lett.*, vol. 7(4), p. 736–740, 2010.
- [5] P. K. Murphy and M. A. Kolodner, "Implementation of a multiscale bayesian classification approach for hyperspectral terrain categorization," *Proc. SPIE*, vol. 48(16), p. 278–287., 2002.
- [6] L. Sun, C. Ma, Y. Chen, Y. Zheng, and B. Jeon, "Low rank component induced spatial-spectral kernel method for hyperspectral image classification," *IEEE Trans. Circuits Syst. Video Technol.*, vol. 30(10), p. 3829–3842, 202.
- [7] Y. Qian, M. Ye, and J. Zhou., "Hyperspectral image classification based on structured sparse logistic regression and three-dimensional wavelet texture features," *IEEE Trans. Geosci. Remote Sens.*, vol. 51(4), p. 2276–2291, 2013.
- [8] L. Shen and S. Jia, "Three-dimensional gabor wavelets for pixel-based hyperspectral imagery classification," *IEEE Trans. Geosci. Remote Sens.*, vol. 49(12), p. 5039–5046, 2011.
- [9] S. Jia, J. Hu, Y. Xie, and L. Shen, "Gabor cube selection based multitask joint sparse representation for hyperspectral image classification," *IEEE Trans. Geosci. Remote Sens.*, vol. 54(6), p. 3174–3187, 2016.
- [10] W. Hu, Y. Huang, L. Wei, F. Zhang, and H. Li, "Deep convolutional neural networks for hyperspectral image classification," *J. Sensors*, vol. 2015, p. 258619, 2015.
- [11] L. Mou, P. Ghamisi, and X. X. Zhu, "Deep recurrent neural networks for hyperspectral image classification," *IEEE Trans. Geosci. Remote Sens.*, vol. 55(7), p. 3639–3655, 2017.
- [12] Y. Li, W. Xie, and H. Li, "Hyperspectral image reconstruction by deep convolutional neural network for classification," *Pattern Recognit.*, vol. 63, p. 371–383, 2017.
- [13] D. Meng, Z. Xu, and J. Paisley, "Hyperspectral image classification with markov random fields and a convolutional neural network," *IEEE Trans. Image Process.*, vol. 27(5), p. 2354–2367, 2018.
- [14] S. Hao, W. Wang, Y. Ye, and E. Li, "A deep network architecture for super-resolution-aided hyperspectral image classification with classwise loss," *IEEE Trans. Geosci. Remote Sens.*, vol. 56(8), p. 4650–4663, 2018.
- [15] J. Feng, H. Yu, L. Wang, X. Cao, X. Zhang, and L. Jiao, "Classification of hyperspectral images based on multiclass spatial-spectral generative adversarial networks," *IEEE Trans. Geosci. Remote Sens.*, vol. 57(8), p. 5329–5343, 2019.



- [16] S. Ghaderizadeh and D. Abbasi-Moghadam, "Hyperspectral image classification using a hybrid 3d-2d convolutional neural networks," in *IEEE Journal of Selected Topics in Applied Earth Observations and Remote Sensing*, vol. 14, pp. 7570–7588, 2021.
- [17] "Hyperspectral imaging in agriculture: opportunities benefits and future perspectives (gamaya.com)," 2021.
- [18] "https://www.globalsecurity.org/intell/library/imint/hyper.htm."
- [19] A. Wania and C. Weber, "Hyperspectral imagery and urban green observation," *Urban Remote Sensing Joint Event*, pp. 1–8, 2007.
- [20] J. Koenig and L. Gueguen, "A comparison of land use land cover classification using super spectrall worldview-3 vs hyperspectral imagery," *Workshop on Hyperspectral Image and Signal Processing: Evolution in Remote Sensing (WHISPERS)*, pp. 1–5, 2016.
- [21] "https://www.esa.int/Applications/Observing_the_Earth/Proba-1/Going_hyperspectral."
- [22] Mateo-Garcia, G. Veitch-Michaelis, and J. Smith, "towards global flood mapping on-board low-cost satellites with machine learning. sci rep 11," *Scientific Rport*, p. 7249, 2021.
- [23] A. K. Singh, R. Sunkara, G. R. Kadambi, and V. Palade, "Spectral-spatial classification with naive bayes and adaptive fft for improved classification accuracy of hyperspectral images," in *IEEE Journal of Selected Topics in Applied Earth Observations and Remote Sensing*, vol. 17, pp. 1100–1113, 2024.
- [24] X. Yang and L. Cheng, "Hyper-spectral image pixel classification based on golden sine and chaotic spotted hyena optimization algorithm," in *IEEE Access*, vol. 11, pp. 89 757–89 768, 2023.
- [25] A. Hamza et al., "An integrated parallel inner deep learning models information fusion with bayesian optimization for land scene classification in satellite images," in *IEEE Journal of Selected Topics in Applied Earth Observations and Remote Sensing*, vol. 16, pp. 9888–9903, 2023.
- [26] J. Feng, et, and al., "Deep reinforcement learning for semi supervised hyperspectral band selection," in *IEEE Transactions on Geoscience and Remote Sensing*, vol. 60, pp. 1–19, 2022.
- [27] S. K. Roy, J. M. Haut, M. E. Paoletti, S. R. Dubey, and A. Plaza, "Generative adversarial minority oversampling for spectral-spatial hyperspectral image classification," in *IEEE Transactions on Geoscience and Remote Sensing*, vol. 60, p. 42005, 2022.
- [28] D. Hong, L. Gao, J. Yao, B. Zhang, A. Plaza, and J. Chanussot, "Graph convolutional networks for hyperspectral image classification," *IEEE Trans. Geosci. Remote Sens.*, vol. 59(7), p. 5966–5978, 2021.
- [29] P. Yang, L. Tong, B. Qian, Z. Gao, J. Yu, and C. Xiao, "Hyperspectral image classification with spectral and spatial graph using inductive representation learning network," in *IEEE Journal of Selected Topics in Applied Earth Observations and Remote Sensing*, vol. 14, pp. 791–800, 2021.
- [30] S. K. Roy, R. Mondal, M. E. Paoletti, J. M. Haut, and A. Plaza, "Morphological convolutional neural networks for hyperspectral image classification," *IEEE Journal of Selected Topics in Applied Earth Observations and Remote Sensing*, vol. 14, p. 8689–8702, 2021.
- [31] R. Hang, Q. Liu, D. Hong, and P. Ghamisi, "Cascaded recurrent neural networks for hyperspectral image classification," in *IEEE Transactions on Geoscience and Remote Sensing*, vol. 57(8), pp. 5384–5394, 2019.
- [32] J. C. Harsanyi and C. I. Chang, "Hyperspectral image classification and dimensionality reduction: an orthogonal subspace projection approach," in *IEEE Transactions on Geoscience and Remote Sensing*, vol. 32(4), pp. 779–785, 1994.
- [33] Te-Ming, T. C.-H. Chen, and C.-I. Chang, "A posteriori least squares orthogonal subspace projection approach to desired signature extraction and detection," in *IEEE Transactions on Geoscience and Remote Sensing*, vol. 35, pp. 127–139, 1997.
- [34] S.Hochreiter and J. Schmidhuber, "Long short-term memory," *Neural computation*, vol. 9(8), p. 1735–1780, 1997.
- [35] F.Melgani and L. Bruzzone, "Classification of hyperspectral remote sensing images with support vector machines," *IEEE Transactions on geoscience and remote sensing*, vol. 42(8), p. 1778–1790, 2004.
- [36] G. Camps-Valls and L. Bruzzone, "Kernel-based methods for hyperspectral image classification," in *IEEE Transactions on Geoscience and Remote Sensing*, vol. 43(6), pp. 1351–1362, 2005.
- [37] J. Ham, Y. Chen, M. M. Crawford, and J. Ghosh, "Investigation of the random forest framework for classification of hyperspectral data," *IEEE Transactions on Geoscience and Remote Sensing*, vol. 43(3), p. 492–501, 2005.
- [38] G. Camps-Valls, L. Gomez-Chova, J. Munoz-Mari, J. Vila-Frances, and J. Calpe-Maravilla, "Composite kernels for hyperspectral image classification," in *IEEE Geoscience and Remote Sensing Letters*, vol. 3(1), pp. 93–97, 2006.
- [39] M. Fauvel, J. A. Benediktsson, J. Chanussot, and J. R. Sveinsson, "Spectral and spatial classification of hyperspectral data using svms and morphological profiles," in *IEEE Transactions on Geoscience and Remote Sensing*, vol. 46(11), pp. 3804–3814, 2008.
- [40] J. Li, J. M. Bio, ucas Dias, and A. Plaza, "Semi supervised hyperspectral image segmentation using multinomial logistic regression with active learning," *IEEE Transactions on Geoscience and Remote Sensing*, vol. 48(11), p. 4085–4098, 2010.
- [41] Y. Chen, N. M. Nasrabadi, and T. D. Tran, "Hyperspectral image classification using dictionary-based sparse representation," in *IEEE Transactions on Geoscience and Remote Sensing*, vol. 49(10), pp. 3973–3985, 2011.
- [42] Y. Chen, Z. Lin, X. Zhao, G. Wang, and Y. Gu, "Deep learning-based classification of hyperspectral data," in *IEEE Journal of Selected Topics in Applied Earth Observations and Remote Sensing*, 7, no. 6, 2094–2107, June 2014, doi: 10.1109/JSTARS.2014.2329330.
- [43] K. Cho, B. V. Merriënboer, D. Bahdanau, and Y. Bengio, "On the " properties of neural machine translation: Encoder-decoder approaches," *arXiv preprint arXiv:1409.1259*, 2014.
- [44] K. Makantasis, K. Karantzas, A. Doulamis, and N. Doulamis, "Deep supervised learning for hyperspectral data classification through convolutional neural networks," in *Proc. IGARSS*, p. 4959–4962, 2015.
- [45] H. Lee and H. Kwon, "Contextual deep cnn based hyperspectral

- classification," *IEEE International Geoscience and Remote Sensing Symposium (IGARSS)*, pp. 3322–3325, 2016.
- [46] Y. Chen, X. Zhao, and X. Jia, "Spectral–spatial classification of hyperspectral data based on deep belief network," in *IEEE Journal of Selected Topics in Applied Earth Observations and Remote Sensing*, vol. 8(6), pp. 2381–2392, 2015.
- [47] D. M. S. Arsa, G. Jati, A. J. Mantau, and I. Wasito, "Dimensionality reduction using deep belief network in big data case study: Hyperspectral image classification," *International Workshop on Big Data and Information Security (IWBIS)*, pp. 71–76, 2016.
- [48] L. Mou, P. Ghamisi, and X. X. Zhu, "Deep recurrent neural networks for hyperspectral image classification," in *IEEE Transactions on Geoscience and Remote Sensing*, vol. 55(7), pp. 3639–3655, 2017.
- [49] X. Zhang, Y. Sun, K. Jiang, C. Li, L. Jiao, and H. Zhou, "Spatial sequential recurrent neural network for hyperspectral image classification," in *IEEE Journal of Selected Topics in Applied Earth Observations and Remote Sensing*, vol. 11(11), pp. 4141–4155, 2018.
- [50] A. Ben, Hamida, A. Benoit, P. Lambert, C. Ben, and Amar, "3-d deep learning approach for remote sensing image classification," *IEEE Transactions on geoscience and remote sensing*, vol. 56(8), p. 4420–4434, 2018.
- [51] Z. Zhong, J. Li, Z. Luo, and M. Chapman, "Spectral–spatial residual network for hyperspectral image classification: A 3-d deep learning framework," in *IEEE Transactions on Geoscience and Remote Sensing*, vol. 56(2), pp. 847–858, 2018.
- [52] S. K. Roy, G. Krishna, S. R. Dubey, and B. B. Chaudhuri, "Hybridsn: Exploring 3-d-2-d cnn feature hierarchy for hyperspectral image classification," *IEEE Geoscience and Remote Sensing Letters*, vol. 17(2), p. 277–281, 2020.
- [53] Lecun, Y. Bottou, L. Bengio, and Y. Haffner, "Gradient-based learning applied to document recognition," *Proceedings of the IEEE*, vol. 86 (11), p. 2278–2324, 1998.
- [54] Krizhevsky, A. Sutskever, and I. Hinton, "Imagenet classification with deep convolutional neural networks. advances in neural information processing systems," *NeurIPS Proceedings*, pp. 1097–1105, 2012.
- [55] He, K. Zhang, and X. Ren, "Deep residual learning for image recognition," *Proceedings of the IEEE conference on computer vision and pattern recognition*, pp. 770–778, 2016.
- [56] Simonyan, K., and Zisserman, "Very deep convolutional networks for large-scale image recognition.," *arXiv preprint arXiv:1409.1556*, 2014.
- [57] Matthew, D. Zeiler, Rob, and Fergus, "Visualizing and understanding convolutional networks," <https://arxiv.org/abs/1311.2901v3>, 2013.
- [58] Szegedy, Christian, Vanhoucke, Vincent, Ioffe, Sergey, Shlens, Jonathon, Wojna, and Zbigniew, "Rethinking the inception architecture for computer vision"," *arXiv:1512.00567v3 cs.CV*, 2015.
- [59] Huang, Gao, Liu, Zhuang, van, der, and Maaten, "Densely connected convolutional networks," *arXiv:1608.06993*, 2016.
- [60] Asifullah, Khan, Anabia, Sohail, Amna, and Ali, "A new channel boosted convolutional neural network using transfer learning"," *arXiv:1804.08528*, 2018.
- [61] Lipton, Z. Kale, D. Elkanet, and al, "Learning to diagnose with lstm recurrent neural networks. international conference on learning representations (iclr)." 2016.
- [62] A. Behera, Z. Wharton, Y. Liu, M. Ghahremani, S. Kumar, and N. Bessis, "Regional attention network (ran) for head pose and fine-grained gesture recognition," in *IEEE Transactions on Affective Computing*, doi: 10.1109/TAFFC.2020.3031841.
- [63] Anand, R. Veni, S, and Aravinth, "Classification technique for hyperspectral images based on 3d-discrete wavelet transform. remote sens. 2021," vol. 13, p. 1255, 2021.
- [64] D. P. Kingma and J. Ba, "Adam: A method for stochastic optimization," <https://arxiv.org/abs/1412.6980v9>, 2014.
- [65] S. Ioffe and C. Szegedy, "Batch normalization: Accelerating deep network training by reducing internal covariate shift," *arXiv:1502.03167*, 2015.
- [66] M.Paoletti, J. Haut, J. Plaza, and A. Plaza, "Deep learning classifiers for hyperspectral imaging: A review," *ISPRS Journal of Photogrammetry and Remote Sensing*, vol. 158, p. 279–317, 2019.



Mr. Rahul K Ghotekar Research Scholar (Pursuing PhD) at Department of Computer Engineering, Kalinga Institute of Industrial Technology, Bhubaneswar, Odisha, India. Completed M.E in Computer Engineering with first Class from Pune University, also completed B.E in Information Technology with distinction from Pune University.



Dr. Kailash Shaw Pune, India born in 1983, and has received his PhD degree in Computer Science & Engineering from SOA University in 2016. He is the author of many research book chapter, more than 45 Peer reviewed articles, and 10 inventions. His research interests include Bio-Informatics, Time Series data forecasting, Bio-Inspired algorithms. He is an Associate Editor of the IJACTE and holds two patents. He is the recipient of the Visweswarya Prativa Puruskar in 2015 and act has resource person and chief guest in many technical events. He is regular reviewer of Elsevier, IEEE, and Inderscience journal.



Dr. Minakhi Rout currently working as Assistant Professor in school of computer engineering, KIIT Deemed to be University. She has recieved M.tech and Ph.D. degree in Computer Science & Engineering from Siksha O Anusandhan University, Odisha, India in 2009 and 2015, respectively. She has more than 13 years of teaching and research

experience in many reputed institutes. Her research interests include Computational Finance, Data Mining and Machine learning. She has published more than 25 research papers in various reputed journals and international conferences as well as guided several M.Tech and Ph.D. thesis. She is an editorial member of Turkish journal of forecasting.